


Article

Mechanisms Driving Recent Sea-Level Acceleration in the Gulf of Guinea

Ayinde Akeem Shola ^{1,2,3}, Huaming Yu ^{1,2,*}, Kejian Wu ^{1,2} and Nir Krakauer ⁴ 

¹ College of Oceanic and Atmospheric Sciences, Ocean University of China, Qingdao 266100, China; ayindeas@niomr.gov.ng (A.A.S.); kejianwu@ouc.edu.cn (K.W.)

² Physical Oceanography Laboratory, Ocean University of China, Qingdao 266100, China

³ Department of Marine Meteorology and Climate, Nigerian Institute for Oceanography and Marine Research, Victoria Island, Lagos PMB 12729, Nigeria

⁴ Department of Civil Engineering, The City University of New York, New York, NY 10016, USA; nkrakauer@ccny.cuny.edu

* Correspondence: hmyu@ouc.edu.cn

Abstract

The Gulf of Guinea is undergoing accelerated sea-level rise (SLR), with localized rates surpassing 10 mm yr^{−1}, more than double the global mean. Integrating GRACE/FO ocean mass data, reanalysis products, and machine learning, we identify a regime shift in the regional sea-level budget post-2015. Over 60% of observed SLR near major riverine outlets stems from ocean mass increase, driven primarily by intensified terrestrial hydrological discharge, marking a transition from steric to barystatic and manometric dominance. This shift coincides with enhanced monsoonal precipitation, wind-forced equatorial wave adjustments, and Atlantic–Pacific climate coupling. Piecewise regression reveals a significant 2015 breakpoint, with mean coastal SLR rates increasing from 2.93 ± 0.1 to 5.4 ± 0.25 mm yr^{−1} between 1993 and 2014, and 2015 and 2023. GRACE data indicate extreme mass accumulation (>10 mm yr^{−1}) along the eastern Gulf coast, tied to elevated river discharge and estuarine retention. Dynamical analysis reveals the reorganization of wind field intensification, which modifies Rossby wave dispersion and amplifies zonal water mass convergence. Random forest modeling attributes 16% of extreme SLR variance to terrestrial runoff (comparable to wind stress at 19%), underscoring underestimated land–ocean interactions. Current climate models underrepresent manometric contributions by 20–45%, introducing critical projection biases for high-runoff regions. The societal implications are severe, with >400 km² of urban land in Lagos and Abidjan vulnerable to inundation by 2050. These findings reveal a hybrid steric–manometric regime in the Gulf of Guinea, challenging existing paradigms and suggesting analogous dynamics may operate across tropical margins. This calls for urgent model recalibration and tailored regional adaptation strategies.

Keywords: sea-level rise; Gulf of Guinea; ocean mass redistribution; terrestrial hydrology; climate teleconnections



Academic Editor: Sergei Badulin

Received: 28 July 2025

Revised: 11 August 2025

Accepted: 11 August 2025

Published: 15 August 2025

Citation: Akeem Shola, A.; Yu, H.; Wu, K.; Krakauer, N. Mechanisms Driving Recent Sea-Level Acceleration in the Gulf of Guinea. *Remote Sens.* **2025**, *17*, 2834. <https://doi.org/10.3390/rs17162834>

Copyright: © 2025 by the authors. Licensee MDPI, Basel, Switzerland. This article is an open access article distributed under the terms and conditions of the Creative Commons Attribution (CC BY) license (<https://creativecommons.org/licenses/by/4.0/>).

1. Introduction

Sea-level rise (SLR) represents one of the most consequential and spatially heterogeneous impacts of climate change, with global mean sea level (GMSL) increasing by approximately 20 cm since 1900. This trend has accelerated by over 60% since 1990 [1]. While GMSL provides a planetary-scale benchmark, regional deviations from this average

often prove more critical for coastal adaptation, particularly in low-lying regions where dynamic oceanic and hydrological processes contribute to the local rates [2]. The Gulf of Guinea (GoG), a densely populated tropical Atlantic basin spanning 12 West African nations (Figure 1), illustrates this disparity: recent altimetry data reveal localized coastal SLR rates exceeding 10 mm/year, more than double the global mean, yet the precise mechanisms driving this acceleration remain unresolved. This knowledge gap impedes evidence-based adaptation for a region where over 30 million people face escalating risks of permanent inundation, saltwater intrusion, and climate-driven displacement [3].

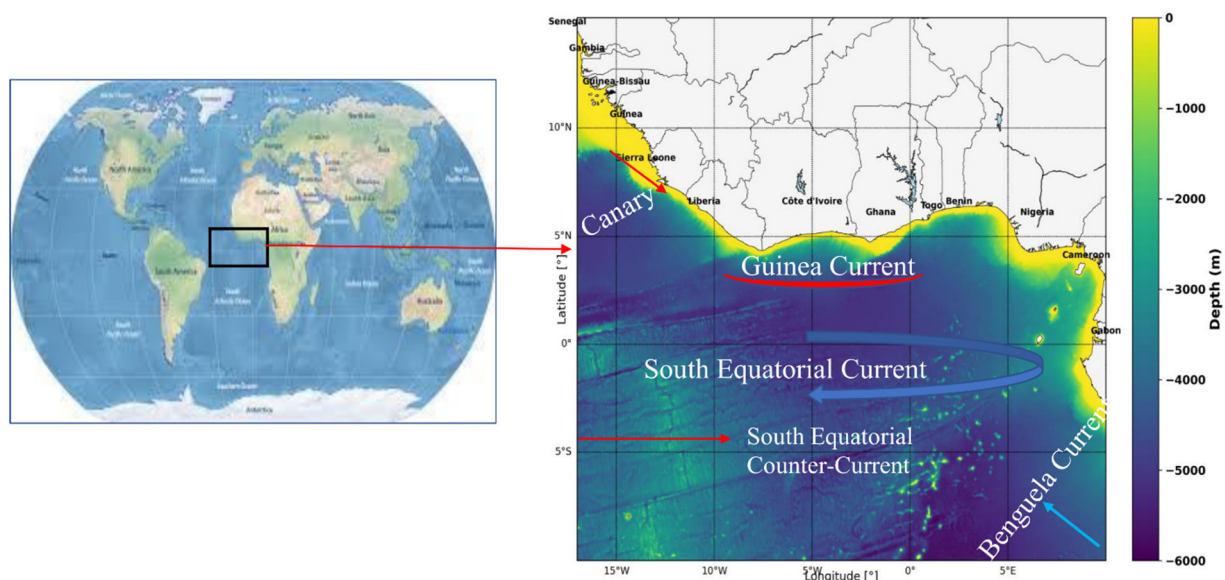


Figure 1. Bathymetric map of the Gulf of Guinea based on the GEBCO 15-arc-second global dataset (<https://www.gebco.net/> accessed on 20 June 2024), showing seafloor depths > 10 m. Major surface currents influencing regional ocean dynamics are overlaid. National boundaries and labels provide geographic context.

Regional SLR is governed by a complex interplay of steric (thermal expansion, salinity changes) and mass-related contributions (barystatic, manometric), exhibiting distinct spatial signatures. In the GoG, the interplay is further modulated by its equatorial location and position across both hemispheres, subjecting it to a mix of equatorial and off-equatorial forcings. The basin is influenced by five major currents, the Canary, Guinea, South Equatorial, Equatorial Counter, and Benguela currents (Figure 1), which regulate thermohaline structure and regional circulation. Its narrow continental shelf (~100 km) amplifies the coastal trapping of dynamic sea-level anomalies [4]. Superimposed on these physical drivers, rapid coastal urbanization, especially in megacities such as Lagos and Abidjan, which is expanding at 3–5% annually, has significantly increased regional vulnerability to rising seas [5]. Despite this clear vulnerability, the current understanding of GoG sea-level variability remains fragmented across traditional research boundaries. Previous studies have examined steric effects [6,7], equatorial Kelvin wave dynamics [8], and climate teleconnections [9] in isolation, without developing a unified framework that captures their interactions. Most critically, the potential role of ocean mass redistribution (OMR), particularly from local mass inputs such as terrestrial runoff, has been largely neglected in regional sea-level assessments, despite the GoG's extensive river systems and changing precipitation regimes. This knowledge gap is particularly concerning given the region's recent acceleration in sea-level rise rates, the physical drivers of which remain poorly understood and underexamined in the literature.

This study addresses that gap using an integrated, multi-platform framework. We combine three decades of satellite altimetry (1993–2023), GRACE/GRACE-FO ocean mass data, capturing both barystatic (global) and manometric (local) mass contributions, reanalysis products, and machine learning to examine the drivers of accelerating sea-level trends in the GoG. We aim to quantify the relative contributions of steric and mass components, identify the mechanisms underlying the observed post-2015 acceleration, and determine whether this shift reflects a fundamental change in the regional sea-level budget. We specifically evaluate how wind stress curl, monsoonal runoff, and Atlantic–Pacific climate teleconnections interact to modulate sea level in the region. Using relevant statistical and machine learning methods, we assess the spatial and temporal evolution of forcing mechanisms and their predictive significance. A central question is whether current global models, designed around steric dominance, adequately capture the land–ocean–atmosphere coupling now emerging in tropical coastal systems.

By addressing these objectives, this study establishes a unified, process-based framework for understanding sea-level rise in the Gulf of Guinea. The approach applies to other low-lying tropical regions experiencing rapid coastal changes that deviate from global trends. The findings enhance understanding of the evolving nature of sea-level change in the region and provide a scientific basis for future projections and coastal risk assessments. Given the socio-economic and environmental vulnerability of West African coastal zones, the results hold relevance for informing climate adaptation strategies and coastal protection planning. This aligns with the IPCC AR6 recommendation for regionally specific, mechanistic assessments to improve adaptation responses to accelerating sea-level risks [10].

2. Data and Methods

The primary dataset used in the study is the monthly sea-level anomaly (SLA) (1993–2023) obtained from CMEMS (product: SEALEVEL_GLO_PHY_L4_REP_OBSERVATIONS_008_047). This dataset integrates multi-mission altimetry observations with corrections for tides, atmospheric pressure, and instrumental biases. Gridded at $1/12^\circ$, the SLA field includes coastal and open-ocean signals. Thermosteric and halosteric components of SLA were derived from EN4 [11] and CMEMS subsurface data using 0–2000 m profiles of temperature and salinity. These components isolate contributions from thermal expansion and salinity-driven density changes, respectively. Ocean heat content (OHC) was computed over the same depth. Glacial isostatic adjustment (GIA) corrections were applied using the ICE-6G_C (VM5a) model [12]. To quantify mass-related contributions, GRACE and GRACE-FO mascon solutions (CSR RL06, $1^\circ \times 1^\circ$ resolution) were used to derive ocean bottom pressure and steric-adjusted mass change from 2002 to 2023 (https://podaac.jpl.nasa.gov/dataset/TELLUS_GRACGRFO_MASCON_CRI_GRID_RL06_V2 accessed on 20 June 2024). Ocean surface forcing variables include wind speed, sea surface temperature (SST), mean sea-level pressure (MSLP), precipitation, evaporation, and runoff from ERA5 and NCEP/NCAR Reanalysis.

2.1. Decomposition of Sea-Level Signal

The spatial linear trends of SLA were computed at each grid point using the OLS regression method. The regression equation used to determine the linear trend at a given grid point is given by:

$$\text{SLA}(t) = \beta_0 + \beta_1 t + \varepsilon_t \quad (1)$$

where $\text{SLA}(t)$ is the sea-level anomaly at time t , β_0 is the intercept, β_1 is the regression coefficient representing the linear trend, and ε_t is the residual term. To test the statistical significance of these trends, the non-parametric MK trend test was employed at a 99%

confidence level [13,14]. The MK test evaluates whether a monotonic trend exists in the time series by computing the test statistic S :

$$S = \sum_{i=1}^{n-1} \sum_{j=i+1}^n \text{sgn}(SLA_j - SLA_i), \quad (2)$$

where $\text{sgn}(SLA_j - SLA_i)$ is defined as:

$$\text{sgn}(SLA_j - SLA_i) = \begin{cases} +1 & \text{if } SLA_j - SLA_i > 0, \\ 0 & \text{if } SLA_j - SLA_i = 0 \\ -1 & \text{if } SLA_j - SLA_i < 0 \end{cases}$$

The magnitude of the trends was estimated using the Theil–Sen slope estimator [15,16], which computes the median of all possible pairwise slopes:

$$\beta = \text{median}f(x) = \left(\frac{SLA_j - SLA_i}{j - i} \right), \quad \forall i < j. \quad (3)$$

This approach is less sensitive to outliers and provides a reliable estimate of the trend magnitude and direction.

The interannual variability was isolated by extracting monthly mean SLA values across the study domain. The climatological mean was removed from the time series to eliminate seasonal effects, and the data were detrended to focus on interannual fluctuations. A 13-month running mean was applied as a low-pass filter to smooth out short-term noise, enabling a clearer focus on long-term patterns:

$$SLA'_t = SLA_t - \frac{1}{N} \sum_{i=1}^N SLA_i - \text{trend}, \quad (4)$$

where SLA'_t is the deseasonalized SLA, SLA_t is the actual SLA, SLA_i is the climatological mean, and N represents the number of years in the dataset. This filtering method isolates interannual variations by smoothing out short-term fluctuations [17].

The seasonal signal was extracted by averaging SLA values for each month across the record at every grid point:

$$SLA_{mm} = \frac{1}{N} \sum_{i=1}^N SLA_{mm,i} \quad (5)$$

where SLA_{mm} is the seasonal mean for month mm , $SLA_{mm,i}$ represents SLA for month mm in year i , and N is the number of years. Furthermore, a basin-wide seasonal signal was extracted by averaging the SLA over the entire study region for each month.

2.2. Spatiotemporal and Frequency Analysis of SLA

EOF analysis decomposed the SLA dataset into dominant spatial patterns EOFs and their corresponding temporal principal components (PCs), reducing dimensionality while identifying key variability modes [18]. The SLA field X was reconstructed as:

$$x = \sum_{k=1}^N EOF_k \times PC_k, \quad (6)$$

where EOF_k represents the k -th spatial pattern, PC_k is its corresponding time series, and N is the number of retained modes. The orthogonal EOFs and uncorrelated PCs ensure distinct separation of variability modes. Following covariance matrix decomposition into eigenvectors and eigenvalues, we analyzed the first few modes that explained most variance for their temporal evolution and spatial coherence. We assess the statistical significance of the explained variance between epochs by conducting a bootstrapping procedure. We resampled the SLA anomalies 1000 times with replacement and performed EOF decomposition on each resampled dataset. The explained variance for each mode

was computed per realization, yielding empirical distributions from which 95% confidence intervals were derived. This approach follows the framework of [19,20], accounting for sampling variability and temporal correlation in SLA fields.

We assessed the persistence of SLA fluctuations using autocorrelation analysis. The lag- k autocorrelation function is:

$$\rho = \frac{\sum_{t=1}^{n-k} (SLA(t) - SLA') (SLA(t+k) - SLA')}{\sum_{t=1}^n (SLA(t) - SLA')^2}, \quad (7)$$

where μ is the mean SLA. The significance was tested using Monte Carlo simulations of red-noise series with matching variance and spectrum. This reveals SLA temporal memory and potential periodicities by quantifying current–past value relationships.

The frequency characteristics of SLA were investigated using power spectral density (PSD) analysis to identify periodic components. PSD was estimated using Welch's method:

$$P(f) = \frac{1}{N} \left| \sum_{t=0}^{T-1} SLA_t e^{-i2\pi f t} \right|^2, \quad (8)$$

where $P(f)$ is the spectral power at frequency f , and T is the number of time steps. This method highlights cyclic patterns such as seasonal and interannual oscillations, offering insight into the dominant frequencies driving SLA variability.

2.3. Nonlinear Modeling and Machine Learning of SLA

Nonlinear variations in SLA were modeled using generalized additive mixed models (GAMMs). These models extend generalized linear frameworks by incorporating smooth functions of predictor variables, allowing for flexible temporal modeling without assuming a predefined shape. The model is expressed as:

$$SLA(t) = \alpha + \sum_{j=1}^P f_j(x_j(t)) + \varepsilon(t) \quad (9)$$

where f_i are smooth functions of predictors $x_j(t)$, and $\varepsilon(t)$ represents the residual error. This structure enables the model to capture complex temporal dynamics in SLA.

Random forest regression (RFR), a supervised machine learning technique, was used to quantify the nonlinear relationships between SLA and its environmental drivers in the GoG. The RFR model was trained on environmental datasets preprocessed using a 13-month running mean and detrending approach. This removed long-term climate variability and enhanced the model's ability to capture shorter-term fluctuations in SLA. The input features included TSA, HSLA, ocean heat content (OHC), wind stress curl (WSC), net heat flux (NHF), precipitation, evaporation, freshwater runoff, and atmospheric pressure. Data were split into training and testing sets using an 80:20 ratio. A grid search method was applied to optimize the hyperparameters and improve model performance, reducing overfitting risk. Once trained, the model learned the underlying relationships and variable interactions driving SLA. Variable importance was assessed using the mean decrease in impurity (MDI) metric. MDI ranks the influence of each predictor by measuring its contribution to impurity reduction across decision trees, highlighting the dominant environmental drivers of SLA in the GoG.

2.4. Ocean Mass Change and Regional Sea-Level Budget Closure

GRACE-FO Level-3 (L3) gridded mass concentration (mascon) data from NASA's Jet Propulsion Laboratory (JPL), specifically the RL06 mascon solution, was used to assess ocean mass change in the Gulf of Guinea. This dataset offers high temporal resolution and improved signal accuracy, enabling detailed monitoring of regional mass anomalies.

We isolated oceanic signals by applying an ocean mask during preprocessing to remove land-based mass variations. GIA corrections were applied using the ICE-6G_C (VM5a) model [12] to account for post-glacial crustal rebound. Further corrections addressed degree-1 (geocenter motion) and degree-2 (Earth's flattening) spherical harmonic terms, which are typically under-constrained in GRACE-derived estimates [21]. Ocean mass variations were derived by converting mascon data into equivalent water height (EWH) using a scaling factor that links mass anomalies to sea-level change [22]. The regional EWH time series was extracted and filtered to reduce noise. Long-term trends in ocean mass change were quantified using OLS regression. Spatial trends were similarly derived at each grid point to map mass change distributions across the study area.

To ensure a closed regional sea-level budget, the geocentric sea-level (RSL) components were reconciled from 2002 to 2023 based on:

$$RSL_{total} - RSL_{GIA} = RSL_{SD} + RSL_{OMR} + RSL_{Res} \quad (10)$$

where RSL_{total} is the observed regional sea-level change, RSL_{GIA} is the contribution from glacial isostatic adjustment, RSL_{SD} represents the sterodynamic component (thermosteric + halosteric), RSL_{OMR} reflects ocean mass redistribution, and RSL_{Res} captures residual terms, VLM, and other unmodeled effects. This framework enables sea-level budget closure over the GRACE/GRACE-FO period and improves understanding of the physical drivers influencing SLR in the GoG. We quantified the ocean mass contribution to SLR by comparing GRACE-derived mass anomalies with contemporaneous altimetry data. The percentage was calculated as $(\Delta\text{Mass}/\Delta\text{SLR}) \times 100$, where ΔMass and ΔSLR represent 13-month running means. Model biases were assessed by differencing CMIP6 ensemble-mean projections from observations. Random forest feature importance was normalized to sum to 100% across all predictors.

3. Results

3.1. Temporal Trends and Physical Attribution

Satellite altimetry analysis reveals a marked acceleration in SLR across the Gulf of Guinea. Piecewise linear regression applied to monthly sea-level anomalies identifies a statistically significant breakpoint in 2015 (Figure 2a). Before this breakpoint (1993–2014), the regional trend averaged 2.93 ± 0.10 mm/year, below the global mean of 3.3 ± 0.3 mm/year [23]. Following 2015, the rate increased sharply to 5.4 ± 0.25 mm/year, exceeding the concurrent global trend of 4.3 mm/year (AVISO, <https://www.aviso.altimetry.fr/en/data/products/ocean-indicators-products/mean-sea-level.html> accessed on 16 February 2024). The full-period linear trend from 1993 to 2023 yields a mean rate of 3.82 ± 0.34 mm/year, consistent with the range of 3.47 to 3.89 ± 0.10 mm/year reported for 1993–2021 by [7] in the region, and confirming the presence of a recent acceleration phase (Figure 2b). This trend aligns with broader global patterns but shows enhanced regional variability. Component decomposition (Figure 2c) illustrates a shift in the dominant contributors to SLR. From 1993 to 2023, sterodynamic processes, primarily thermosteric, contributed an average of 1.24 ± 0.10 mm/year. During the early period of GRACE measurements (pre-2007), the steric trend was higher, measured at 1.71 ± 0.20 mm/year, accounting for approximately 65% of the total sea-level rise. This trend subsequently slowed, approaching zero, and remained nearly stagnant for eight years before peaking in 2015. Between 2002 and 2023, thermosteric contributions increased slightly to 1.36 ± 0.28 mm/year, while halosteric effects added 0.21 ± 0.13 mm/year. In contrast, the OMR component exhibited a significant increase. GRACE/GRACE-FO mascon solutions estimate an OMR contribution of 1.92 ± 0.42 mm/year between 2002 and 2023, exceeding the regional steric

contribution over the same interval. This estimate closely aligns with but remains slightly below the 2.6 mm/year value reported by [24] for the same region and period (2002–2023). The residual term, accounting for vertical land motion (VLM) and other unmodeled signals, explained approximately 0.53 mm/year.

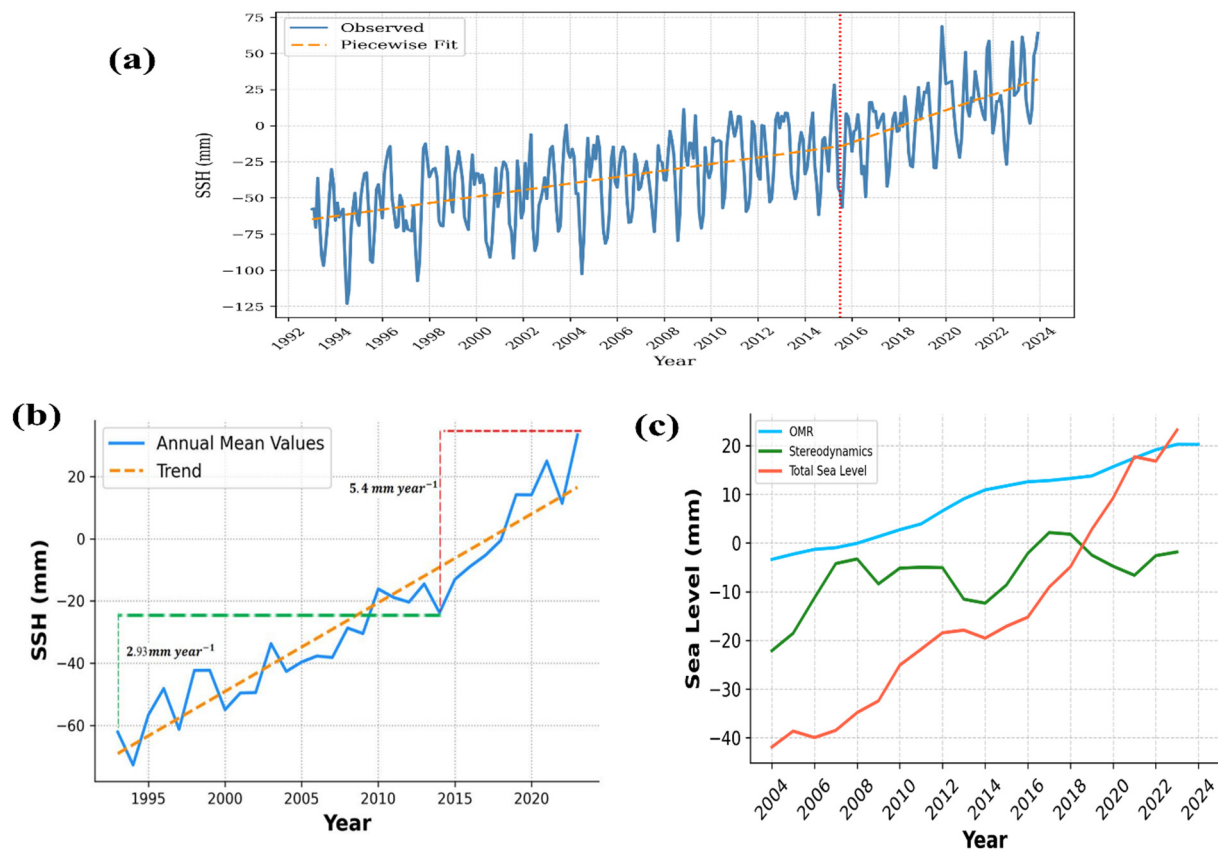


Figure 2. Temporal evolution and component attribution of sea-level change in the Gulf of Guinea. (a) Pettitt test applied to monthly altimetry data (1993–2023) identifies a statistically significant breakpoint in 2015 ($p < 0.01$), indicating a regime shift in SLR trajectory as shown by the red dotted line (b) Spatially resolved SLR trends derived from CMEMS gridded altimetry reveal contrasting regimes between 1993 and 2014 (green dotted line), and 2015 and 2023 (red dotted line), consistent with the identified breakpoint. (c) Long-term SLR (red) decomposed into ocean mass (blue; GRACE-FO) and stereodynamic components (green; altimetry) over 2002–2023. All series were smoothed using a 3-year moving average.

The GAMM model fitted to the deseasonalized SLA time series from 1993 to 2023, using a B-spline basis, effectively captures the low-frequency structure of the trend while preserving high-frequency variability in the observed data (Figure 2a). The model identifies distinct nonlinear phases, including a sustained negative anomaly during the 1990s, near-zero anomalies around 2008, and a pronounced acceleration in sea-level rise following 2015, indicating a significant shift in the long-term SLA trajectory. This nonlinear characteristic of SLA reflects temporally heterogeneous drivers, with dominant factors varying over time. The post-2015 inflection coincides with enhanced wind stress curl variability, supporting the interpretation of a dynamical transition in regional sea-level drivers. Model residuals (Figure 3B) exhibit a symmetric, near-normal distribution with no apparent skewness or kurtosis. The absence of autocorrelation or heteroscedasticity indicates that the GAMM effectively isolates the deterministic trend, leaving residuals consistent with stochastic variability. Temporal diagnostics further support the presence of structured variability. The autocorrelation function (ACF; Figure 4a) shows significant persistence at 12-, 24-, and

36-month lags, indicating seasonal and triennial memory. The first-lag autocorrelation exceeds 0.9, confirming strong internal continuity in SLA dynamics. These patterns suggest modulation by both seasonal and interannual forcing. The power spectral density (PSD; Figure 4b) quantifies periodic components. A dominant annual peak, marked by a sharp spectral spike, reflects dynamic steric and mass-driven changes associated with regional hydrodynamic cycles. The sub-annual spectral peak and its adjacent trough indicate the presence of sub-seasonal oscillatory forcing, characterized by distinct high- and low-frequency components associated with ENSO variability and the West African Monsoon (WAM). The intervening spectral slope follows a red-noise pattern, reflecting integrative system dynamics consistent with oceanic memory effects that modulate intra-annual sea-level variability. The final spectral peak, marked by a green dashed line near the decadal band (~ 10 years), indicates the presence of low-frequency variability, such as the Atlantic Multidecadal Oscillation (AMO), embedded within the regional sea-level signal.

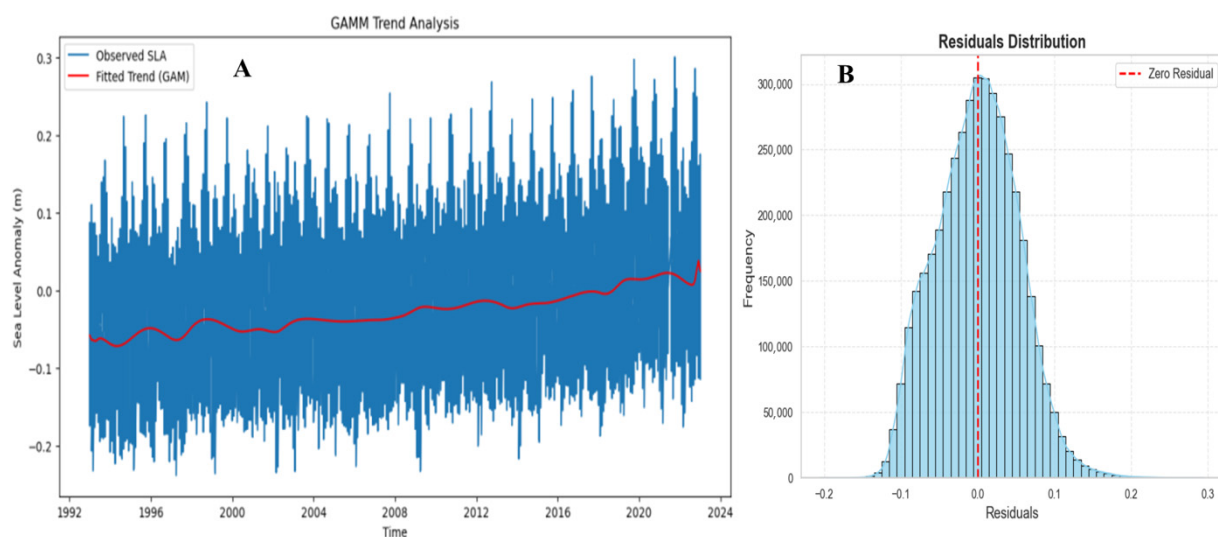


Figure 3. The observed SLA (blue line) with the fitted trend using B-spline smoothing (red line) from the generalized additive mixed model (GAMM) (A); the residual distribution from the model, represented as a histogram (sky blue) with an overlaid kernel density estimate (KDE) curve, highlighting the residual pattern (B).

3.2. Spatial Disaggregation and Forcing Shifts

Spatial trends in sea level and its components, based on OLS regression analysis, reveal notable differences between the pre- and post-2015 periods (Figure 5). During 1993–2014, sea-level rise exhibited a coherent spatial pattern, with moderate increases of approximately 2.7 mm/year across the equatorial Atlantic (Figure 5a–c). Enhanced trends were observed toward the western Gulf of Guinea, particularly near the Bight of Benin and along the Cameroonian coast, where values reached up to 3.8 mm/year. OMR contributions remained relatively low along the immediate coastline (~ 1.0 mm/year) but increased offshore (~ 2.5 mm/year), suggesting barystatic dominance during this period. The steric component exhibited a meridional gradient, with values rising from approximately 1.0 mm/year in the southern basin to 3.0 mm/year along the northern shelf.

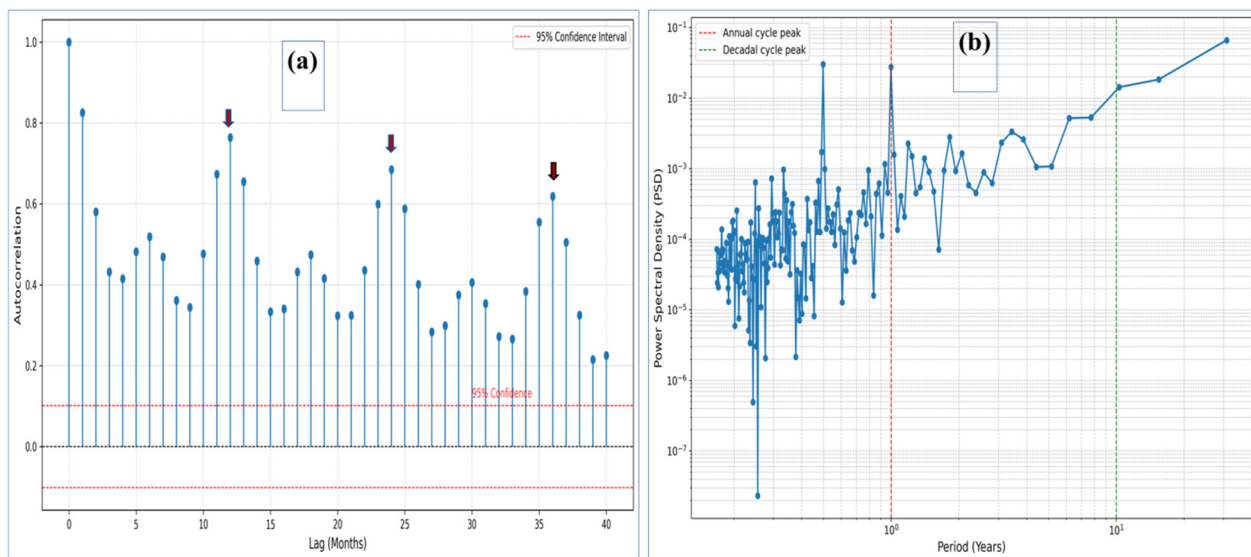


Figure 4. The autocorrelation function (ACF) of mean SLA values over 40 monthly lags highlights significant peaks at 12, 24, and 36 months (red–blue arrows). The black dashed line represents zero autocorrelation, while the red dashed lines denote the 95% confidence interval. The gradual decay of autocorrelation values indicates the persistence of temporal correlations (a). The power spectral density (PSD) of SLA shows variance distribution across log-scaled periods (x-axis, in years) and PSD values (y-axis). Log-period scaling, following oceanographic convention, enhances resolution of seasonal to decadal variability and highlights dominant climate modes (b).

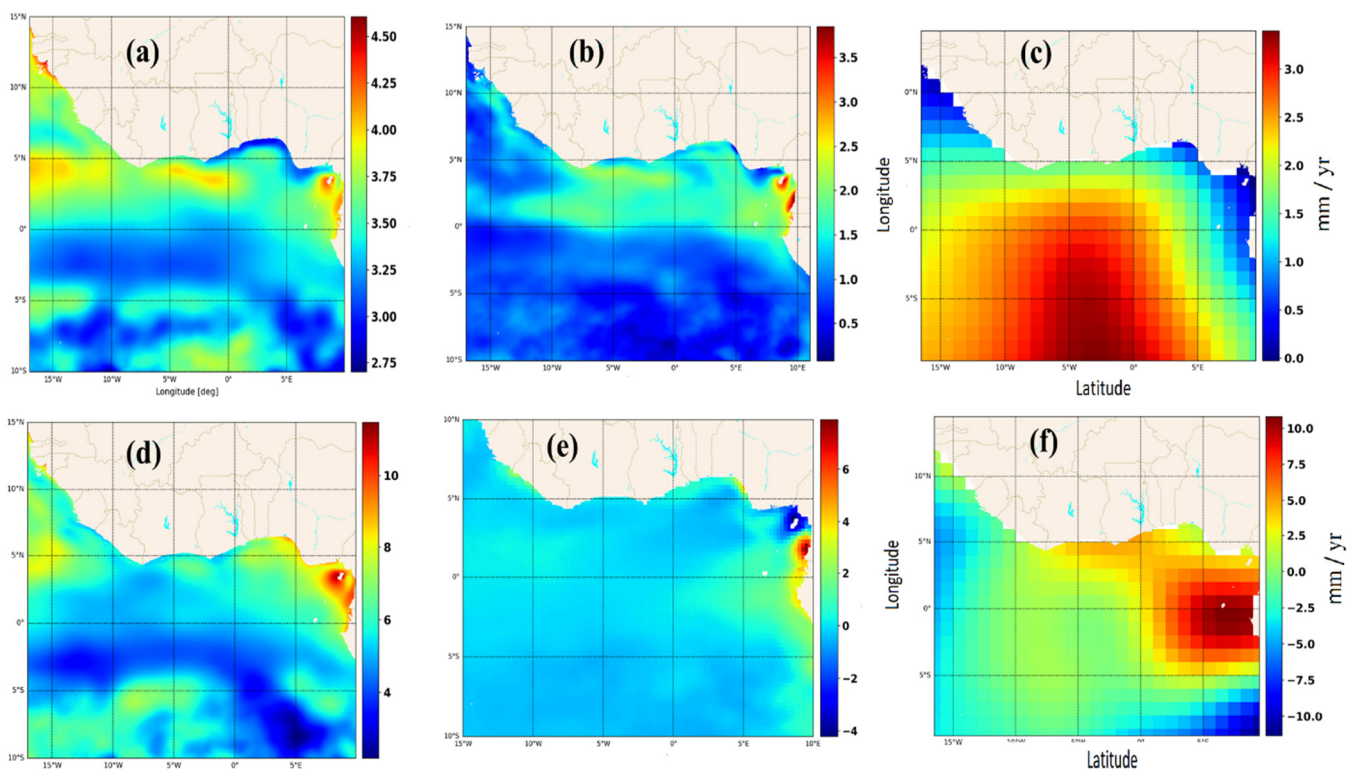


Figure 5. Linear sea-level trends derived from the ordinary least squares (OLS) method, illustrating spatial variability across the Gulf of Guinea. (a) OMR trend (2002–2023), highlighting its strong influence in the southern basin. (b) Sterodynamic sea-level change (1993–2023), showing its dominance in the northern Gulf. (c) Sea-level anomaly (SLA) trend (1993–2023) reveals variability and rapid acceleration along the northern basin. (d–f) Recent linear trends for 2015–2023: (d) OMR, (e) sterodynamic sea level, and (f) SLA, which exceeds the global mean sea level (GSML).

In contrast, from 2015 to 2023, SLR in the Gulf of Guinea intensified and became more spatially heterogeneous (Figure 5d–f). Localized coastal SLR rates reached ~ 10 mm/year along the eastern coasts (particularly off Cameroon/Equatorial Guinea), contrasting with offshore rates < 5 mm/year. This increase reflects stronger contributions from both mass and steric components. OMR trends reveal a spatial reorganization, marking a transition from earlier barystatic dominance to emerging manometric control. Significant positive values were observed along the Niger Delta, Bight of Benin, and Gabon coasts, indicating increased coastal mass accumulation. This pattern likely results from elevated runoff or shifts in regional circulation. Sterodynamic trends became more uniformly distributed than in the earlier period but showed higher values along the same eastern coastal corridor, ranging from 4.0 to 6.0 mm/year. This steric intensification implies stronger thermal expansion and potential coupling with mass-driven processes. The spatial coincidence of elevated OMR and sterodynamic trends after 2015 indicates increased coupling between terrestrial hydrological input and oceanic processes, contributing to the observed recent increase in sea-level rise in the GoG.

The EOF analysis of SLA reveals consistent spatial patterns in the leading three modes for 1993–2014 and 2015–2023, with notable shifts in explained variance (Figure 6a,b). Between 1993 and 2014, EOF1 explained 56.76% of the total variance and captured a dominant eastward-propagating SLA signal from the equatorial Atlantic into the Gulf of Guinea, driven by equatorial Kelvin waves (EKWs) transitioning into coastal trapped waves (CTWs) upon shelf interaction, leading to elevated sea levels at the coast. EOF2 (18.58%) exhibited an equatorial westward-propagating reflected Rossby wave (RRW) structure associated with coastal sea-level depression and enhanced SLA in both hemispheres, influenced by regional current dynamics. EOF3 (11.27%) displayed a dipolar structure centered off the equatorial coast and the southern Gulf of Guinea, consistent with the spatial signature of AMOC variability.

During 2015–2023, the three leading EOF modes retained their spatial structures, indicating persistence of the underlying dynamical processes. EOF1 (57.95%) preserved its coastal-dominant pattern, with enhanced coherence along the central Gulf of Guinea, suggesting a more organized large-scale coastal response. EOF2 (16.09%) also retained its RRW-like structure but exhibited a statistically significant decline in explained variance compared to the earlier period (16.31%). This change was evaluated using 1000 bootstrap realizations, which yielded non-overlapping 95% confidence intervals: [15.42%, 16.95%] for 1993–2014 and [12.87%, 14.83%] for 2015–2023 (Figure 6d). The separation between these intervals confirms that the ~ 2.7 percentage point reduction in explained variance is statistically significant. This decline suggests a weakening of the RRW's contribution to sea-level variability, consistent with reduced offshore transport and diminished coastal sea-level depression. Since RRWs typically push water away from the coast, their reduced variability during the later period implies weaker offshore flux, which would favor local SLA amplification. The persistence of the RRW-like structure despite reduced explained variance indicates continued activity of the mechanism with diminished energy contribution. This attenuation likely reflects a reorganization of equatorial wind stress, with increasingly zonal and coastward orientation (See Figure 10(a1,a2) for details), suppressing westward RRW propagation. Concurrent modifications in wave–mean flow interactions and reduced thermocline tilting may have further limited basin-scale adjustment processes, leading to a weaker dynamical imprint on interannual SLA variability. EOF3 (11.64%) remained structurally similar, but with a more pronounced off-equatorial signal in the southeastern basin, potentially linked to evolving large-scale forcing. The strengthening of EOF1 and concurrent weakening of EOF2 during 2015–2023 coincide with the observed

regional sea-level rise, indicating that reduced interannual offshore energy export via RRW dynamics may have contributed to the sustained coastal SLA increase in the Gulf of Guinea.

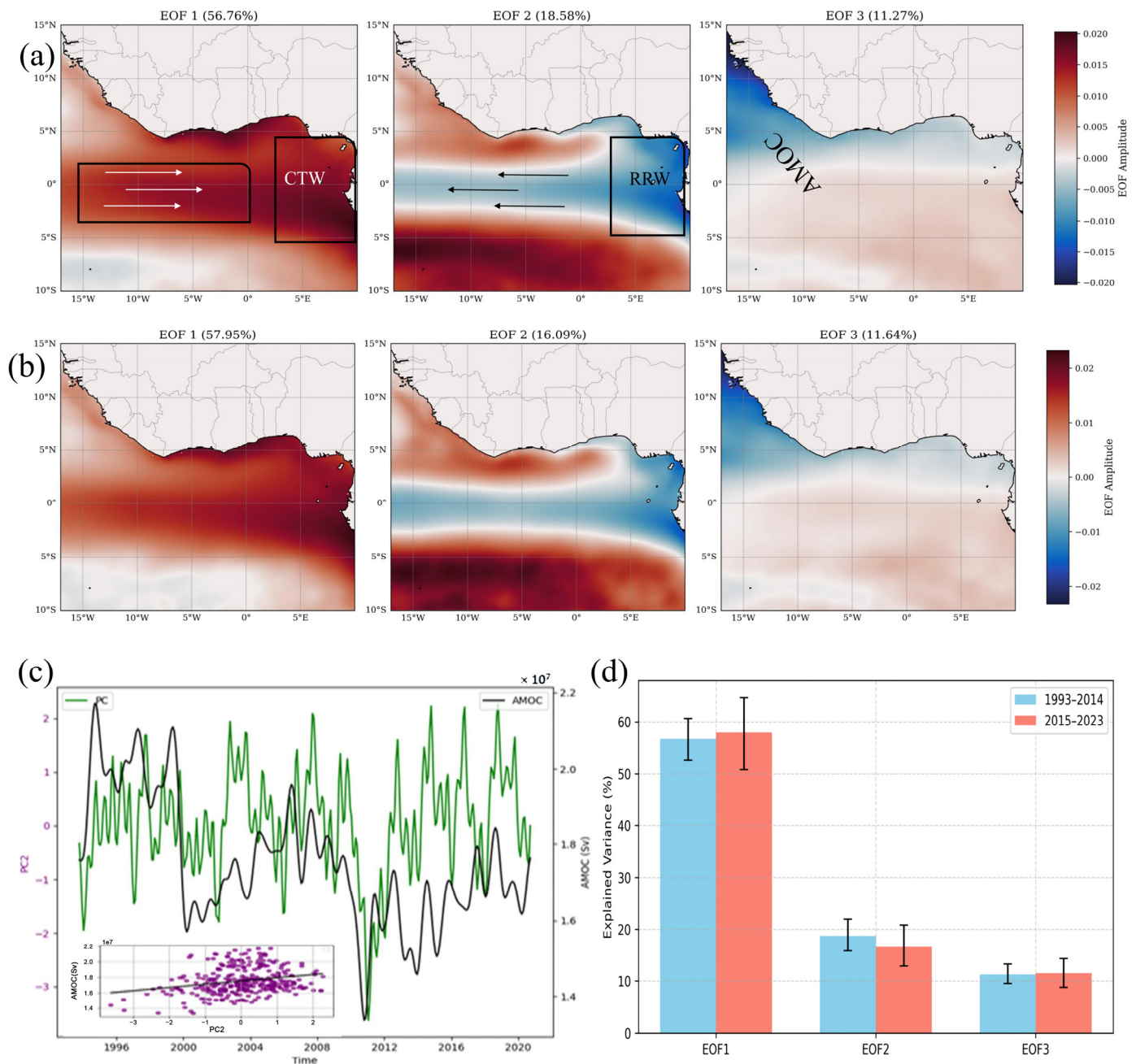


Figure 6. Leading empirical orthogonal function (EOF) modes of interannual SLA variability in the Gulf of Guinea (GoG) highlighting dynamic sea-level changes across two periods. **(a)** First three EOF modes for 1993–2014, explaining 57%, 19%, and 11% of the total variance. **(b)** First three EOF modes for 2015–2023, explaining 59%, 16%, and 12% of the variance. **(c)** Trend and correlation between the principal component of the third EOF mode (PC3) and the Atlantic Meridional Overturning Circulation (AMOC) index (1993–2021). **(d)** Bottom bar plots show 95% confidence intervals obtained from 1000 bootstrap resamples, quantifying variance uncertainty. Black boxes indicate regions of high variability, and arrows denote the primary wave propagation directions of the water masses.

The physical drivers of the leading EOF modes were resolved through combined spectral and Hovmöller analyses of equatorial SLA variability. The 2D power spectrum reveals a dominant westward-propagating Rossby wave signal with a 60-day periodicity (0.0167 cycles/day) and a 30° wavelength, consistent with first baroclinic-mode dynamics

(Figure 7a). This spectral signature was contextualized using two complementary Hovmöller representations: detrended SLA ($\pm 5^\circ\text{N}$) captured eastward-propagating Kelvin waves at theoretical phase speeds of 2.8 m/s, phase-locked with major El Niño events (Figure 7b). At the same time, raw SLA ($\pm 2^\circ\text{N}$) resolved the full amplitude of the subsequent westward-propagating Rossby waves (~ 0.6 m/s) generated via boundary reflection (Figure 7c). The tandem diagnostics show how equatorial Atlantic Kelvin waves, evident in the processed Hovmöller plots during ENSO events (1997–1998, 2009–2010, 2019–2020), reflect into Rossby waves that dominate EOF2’s intraseasonal variability and spatial pattern, particularly between 5°W and 10°E . These wind-forced wave dynamics operate alongside slower AMOC-related influences ($r = 0.51$ with the AMOC index, $p < 0.01$ in PC3 of EOF3) (Figure 6c), demonstrating that regional SLA variability results from the superposition of fast equatorial wave adjustments and thermohaline-driven mass redistribution across timescales. Although earlier studies have attributed SLA variability in the Gulf of Guinea to equatorial Kelvin wave propagation [6,7,25,26] and to AMOC-related forcing in the broader Atlantic basin [27,28], to the best of our knowledge, no study has explicitly linked westward-propagating Rossby waves to SLA variability in the Gulf of Guinea.

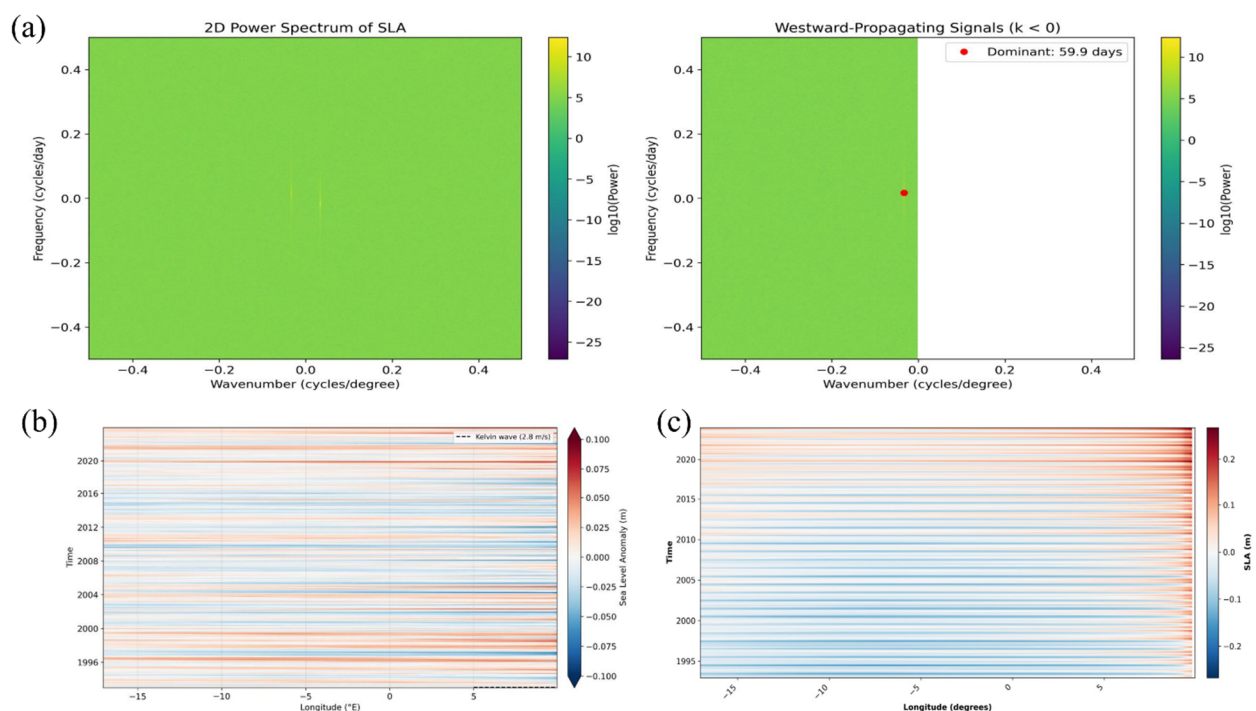


Figure 7. (a) Two-dimensional power spectral density of SLA along the equatorial band (5°S – 5°N), derived from fast Fourier transform (FFT) analysis. The left panel shows log-scaled spectral power as a function of frequency (cycles/day) and zonal wavenumber (cycles/degree); the right panel isolates westward-propagating signals (negative wavenumbers, $k < 0$). The red marker highlights the dominant mode with a 59.9-day period and $\sim 30^\circ$ wavelength, consistent with first-mode equatorial Rossby wave dynamics. (b) Hovmöller diagram of equatorial SLA showing eastward-propagating features. Horizontal dashed lines indicate the theoretical phase speed (2.8 m/s) of first-mode baroclinic Kelvin waves. (c) Hovmöller diagram emphasizing westward-propagating SLA signals. Diagonal trajectories align with the spectral mode identified in (a), supporting the presence of Rossby wave activity across the equatorial Atlantic.

The RFR model precisely reconstructs SLA variability from 1993 to 2023, capturing both interannual peaks and low-frequency trends with high skill (Figure 8a). Model predictions closely track observed SLA, yielding $R^2 = 0.97$ with minimal residual error, demonstrating strong temporal generalization. Feature importance analysis (Figure 8b)

highlights surface currents and WSC as dominant predictors, contributing 21% and 19%, respectively. Hydrological drivers such as terrestrial runoff (16%) and evaporation (11%) also exert a substantial influence. Thermal variables, including TSLA, NHF, and HSLA, contribute less than 10% each. The dominance of dynamical features aligns with the physical mechanisms identified in EOF modes 1 and 2, reflecting the influence of EKW, CTWs, and RRWs on SLA variability. Runoff acts as a significant regional driver of coastal SLA variability, especially along segments influenced by spatially coherent rainfall patterns and major river discharges.

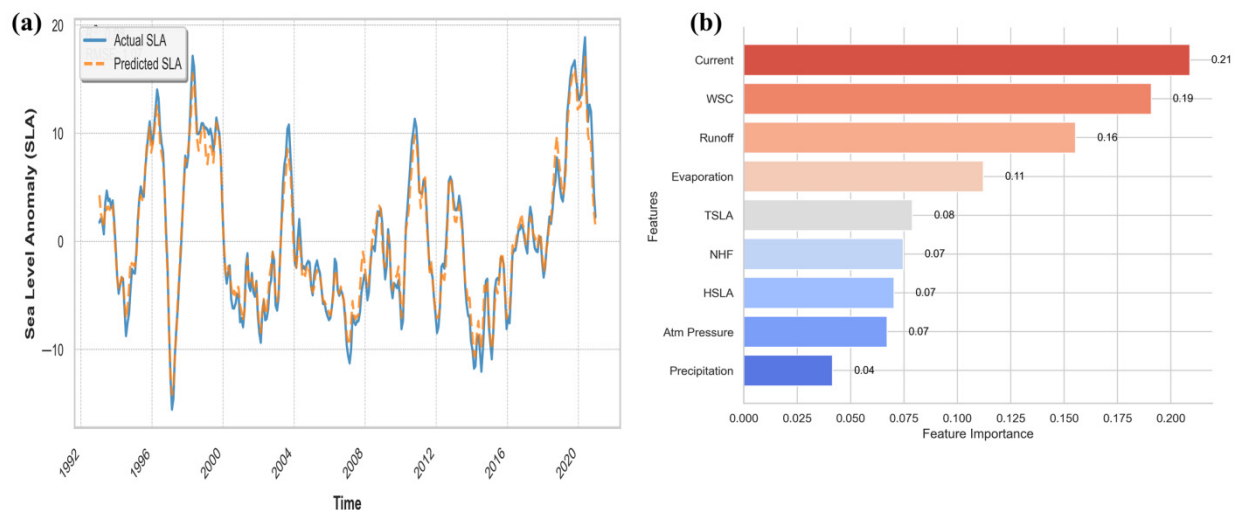


Figure 8. The comparison between the observed SLA (solid blue line) and the predicted SLA (dashed orange line) is derived using a random forest regression (RFR) model with forcing variables as predictors (a). The feature importance of the RFR model, displayed as a horizontal bar chart, illustrates the magnitude of the contribution of each predictor to the model (b). Adapted from Ayinde et al., 2023 [6].

EOF decomposition of atmospheric forcing fields reveals a structural reorganization between the early (1993–2014) and recent (2015–2023) epochs (Figure 9). During 1993–2014, eastward-propagating zonal wind anomalies dominated, with amplitude diminishing toward the eastern basin, favoring EKW generation. Post-2015, zonal wind anomalies intensified and expanded spatially across the equatorial belt while maintaining their fundamental dynamical symmetry (Figure 9(a2)). Concurrently, precipitation shifted from a meridionally diffuse to an equatorially concentrated pattern (Figure 9(b1,b2)). Statistical analysis confirms the primary influence of zonal wind stress (PC1) and runoff on SLA variability ($r = 0.69$ and $r = 0.63$, respectively). Precipitation shows a moderate, episodic correlation with SLA ($r = 0.51$), reflecting a secondary mechanistic role. Although precipitation's direct association with SLA is moderate, its influence operates both locally through immediate runoff and upstream via catchment discharge, rendering it an effective proxy for the basin-integrated hydrological flux that modulates coastal sea-level variability. Lagged correlations reveal distinct response timescales: SLA anomalies lag wind PC1 by 2–4 months (peak $r \approx 0.45$), consistent with ocean adjustment through baroclinic wave dynamics, whereas precipitation–SLA coupling peaks at zero lag ($r \approx 0.57$), indicating an immediate hydrological response (Figure 9c).

Linear trends in wind speed and direction reveal a clear atmospheric shift between 1993 and 2014, and 2015 and 2023 (Figure 10(a1,a2)). The earlier period featured modest offshore wind strengthening, dominated by meridional flow and weak divergence along the northern coast. After 2015, winds intensified zonally along the eastern Gulf of Guinea, with stronger equatorward and eastward components indicating large-scale circulation

changes. This reorganization aligns with the emerging SLA pattern along the eastern margin, where strengthened zonal wind stress opposes RRW propagation. The resulting water mass convergence drives accelerated coastal sea-level rise, consistent with observed post-2015 SLA trends (Figures 5d, 6b and 10(a2)).

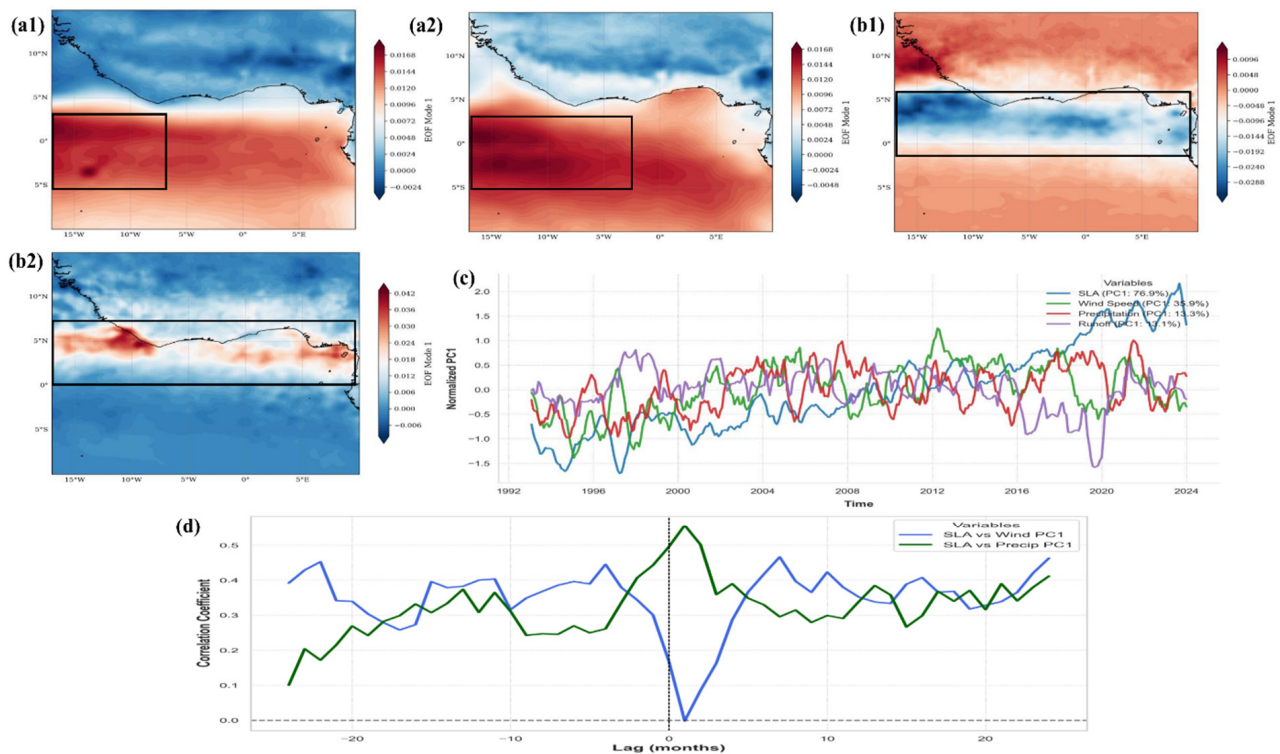


Figure 9. First empirical orthogonal function (EOF1) modes of zonal wind stress and precipitation over the Gulf of Guinea, shown separately for two periods: (a1,a2) zonal wind EOF1 spatial patterns for 1993–2014 and 2015–2023; (b1,b2) precipitation EOF1 spatial patterns for 1993–2014 and 2015–2023. (c) Normalized time series of PC1 for wind and precipitation, alongside total runoff, compared with regional SLA anomalies from 1993 to 2023. (d) Cross-correlation functions between SLA and wind PC1 (blue), and SLA and precipitation PC1 (green), showing leading–lagging relationships. Black boxes highlight regions of highest variability, except in (b1), which denotes regions of lowest variability.

Precipitation trends show contrasting patterns between epochs. From 1993 to 2014 (Figure 10(b1)), rainfall anomalies were weak and spatially incoherent. In 2015–2023 (Figure 10(b2)), a pronounced wetting trend exceeding +6 mm/year emerges along the eastern coast, including the Niger Delta, Bight of Benin, and coastal Cameroon. This regional intensification coincides with enhanced wind convergence zones (Figure 10(a2,b2)) and rising sea levels (Figure 5d), suggesting links to monsoonal strengthening or a southward shift of the Intertropical Convergence Zone (ITCZ). Seasonal WSC variability clarifies these dynamics (Figure 10c). DJF exhibits weak cyclonic anomalies, indicating a quiescent wind regime with minimal upwelling. MAM shows moderate negative curl anomalies west of Nigeria, favoring downwelling conditions. JJA is marked by strong positive curl anomalies between 5°S and the equator, driving Ekman divergence and reinforcing coastal upwelling; this pattern persists, though weaker, into SON. These seasonal WSC patterns align with previously documented upwelling cycles in the region [29,30], underscoring the tightly coupled ocean–atmosphere interactions that regulate sea-level variability and marine productivity in the Gulf of Guinea.

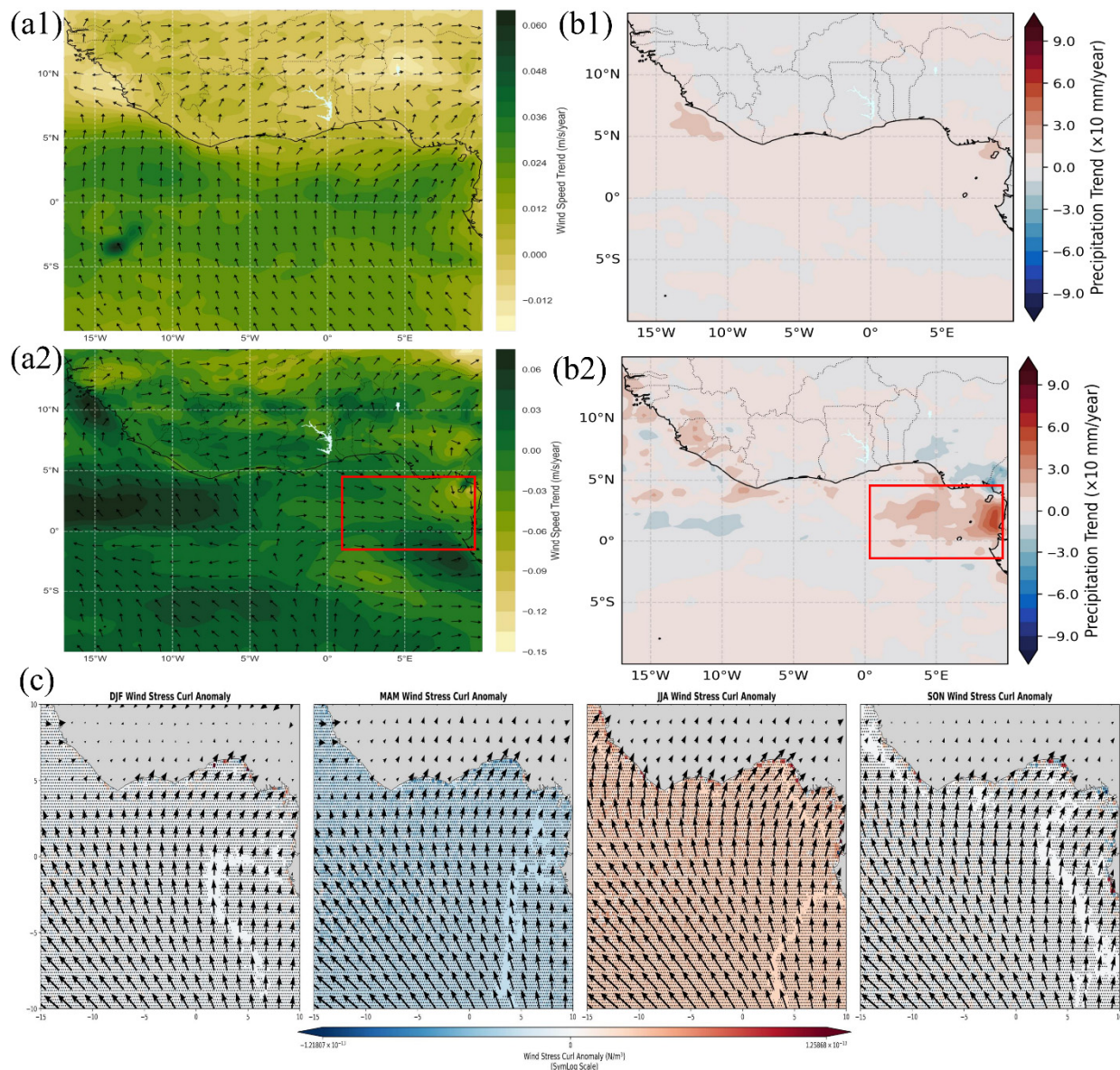


Figure 10. Linear trends in surface wind and precipitation over the Gulf of Guinea during two periods: (a1,a2) wind vector magnitude and direction trends for 1993–2014 and 2015–2023; (b1,b2) precipitation trends for 1993–2014 and 2015–2023. Red boxes indicate regions of statistically significant change, highlighting zones of recent intensification in atmospheric dynamics. (c) Cross-correlation functions between SLA and wind PC1 (blue), and SLA and precipitation PC1 (green), showing lagged responses and temporal coupling with sea-level variability.

3.3. Climate Variability and Regional Teleconnections

3.3.1. Seasonal SLA Variability and Hydroclimatic Forcing

Seasonal variability in SLA across the GoG reflects a tightly coupled response to regional hydroclimatic forcing. Composite SLA–precipitation fields for DJF, MAM, JJA, and SON (Figure 11a,b) highlight distinct seasonal patterns that correspond with shifts in atmospheric dynamics and freshwater flux. SON exhibits the strongest positive SLA anomalies along the northern coastal margin, coinciding with peak rainfall in the region. This alignment indicates a strong coupling between SLA and the West African Monsoon (WAM) system during late boreal summer to early autumn [31,32]. During JJA, the northward migration of the ITCZ intensifies southwesterly low-level winds, which drive increased precipitation over coastal West Africa. Enhanced freshwater input from direct precipitation,

fluvial discharge, and catchment runoff raises local sea levels through ocean mass loading and dynamic adjustment. During SON, sustained rainfall, river overflow, and reduced soil infiltration, resulting from antecedent soil moisture saturation, maintain elevated runoff, reinforcing coastal SLAs. This cumulative hydrological forcing sustains high SLA anomalies into the late monsoon season, with sea levels along the coast.

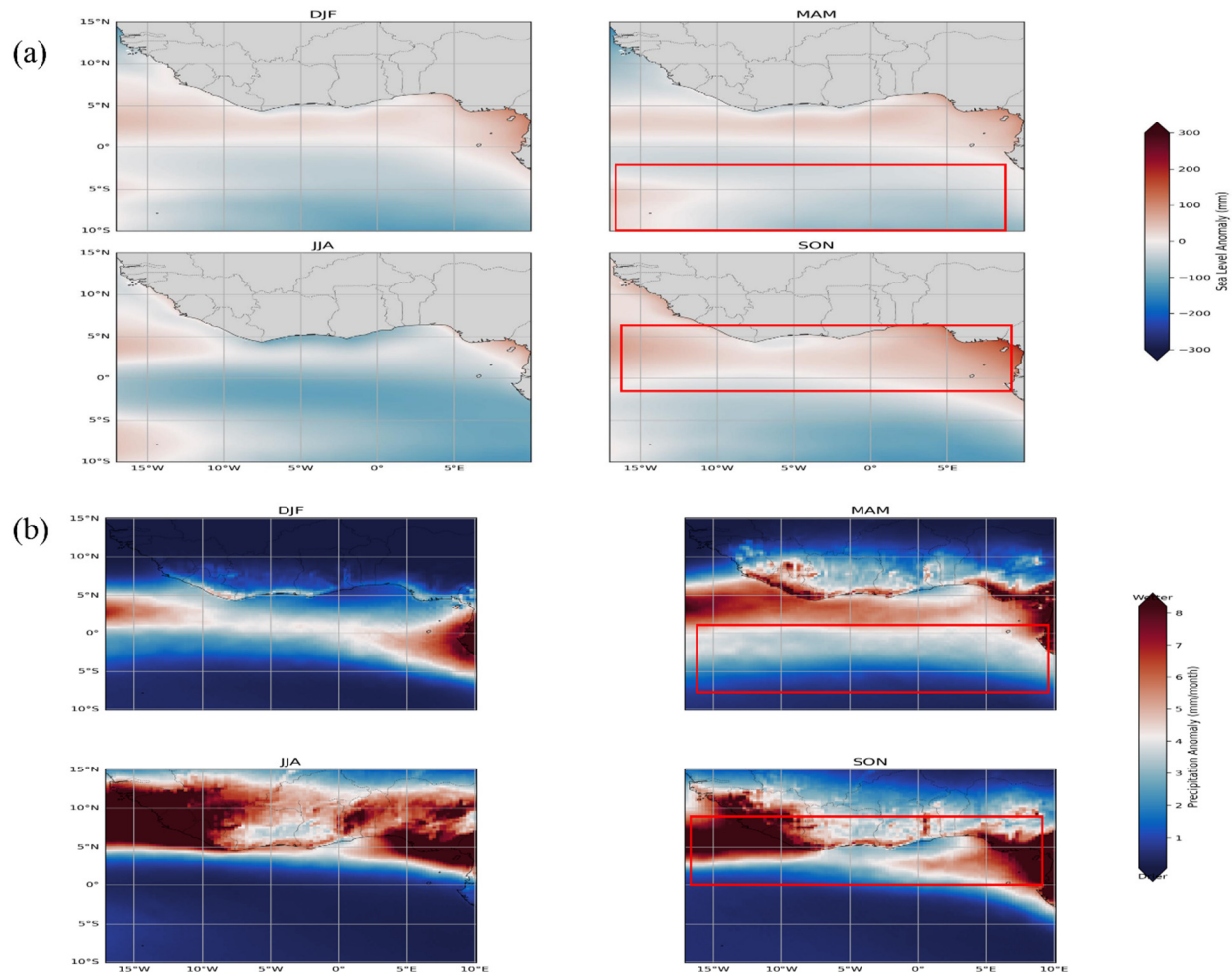


Figure 11. Spatial trends in seasonal variability of (a) sea-level anomaly (SLA) and (b) precipitation across the Gulf of Guinea from 1993 to 2023, derived from monthly mean values at each grid point. The panels reveal strong seasonal heterogeneity between the northern and southern sub-basins. Red boxes indicate zones of pronounced SLA and rainfall divergence, reflecting spatially distinct ocean–atmosphere interactions across the basin.

To assess the relative contributions of thermohaline and mass-driven processes to regional SLA, spatial correlations were computed between SLA and its two dominant components, stericodynamic height (combined steric and dynamic) and OMR, across two epochs: 1993–2014 and 2015–2023. During 1993–2014, SLA showed a strong correlation with stericodynamic height ($r \approx 0.7$) throughout the equatorial and northern GoG (Figure 12(a1)). This spatial pattern matches the leading mode of SLA variability captured in EOF1 (Figure 6a,b), dominated by eastward-propagating equatorial Kelvin waves (EKW) and associated steric effects. The coherence reflects a basin-scale dynamical regime in which wave adjustment redistributes subsurface heat and modulates density structure. Concurrent SLA–OMR correlations range from $r = 0.4$ – 0.6 and are broadly distributed across the basin (Figure 12(b1)). Although weaker than the steric signal, the OMR pattern follows the same zonal structure as the EKW pathway, suggesting complementary hydrological modulation.

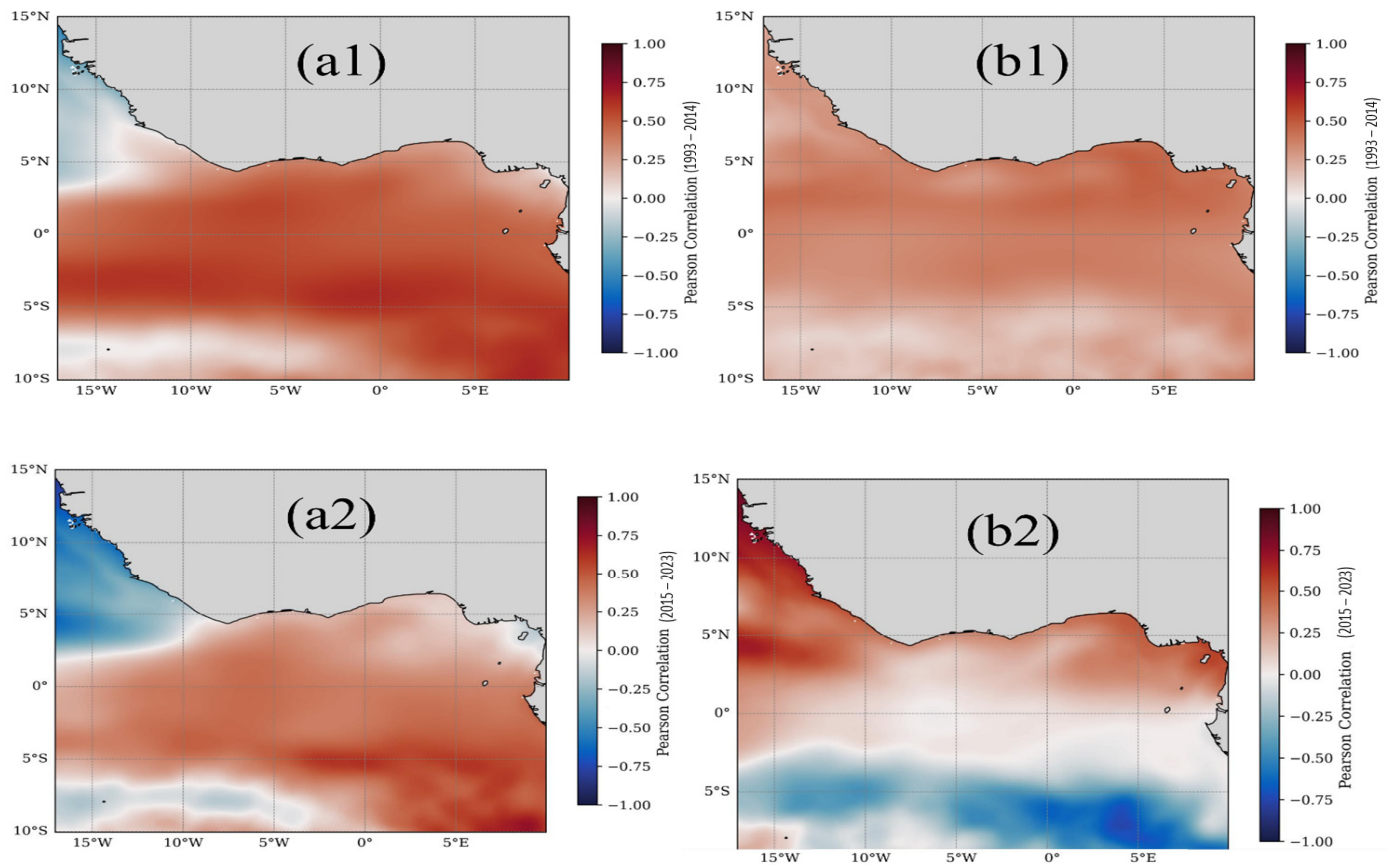


Figure 12. Spatial Pearson correlation between SLA and sterodynamic components for **(a1)** 1993–2014 and **(a2)** 2015–2023, and between SLA and OMR for **(b1)** 1993–2014 and **(b2)** 2015–2023.

The post-2015 period marks a structural shift in SLA forcing. SLA–sterodynamic correlations weaken basin-wide, indicating diminished steric influence (Figure 12(a2)). In contrast, SLA–OMR correlations intensify, particularly in coastal and estuarine zones of the eastern GoG, most notably near the Niger Delta, Bight of Benin, and southern Cameroon. Offshore correlations decline, reflecting a spatial decoupling between large-scale ocean dynamics and coastal SLA variability (Figure 12(b2)). This transition signals a shift toward nearshore dominance, where enhanced precipitation and terrestrial runoff exert stronger control on SLA via localized mass loading. The amplification of OMR influence coincides with post-2015 atmospheric changes: intensified zonal wind stress, low-level convergence, and elevated rainfall (Figures 5f, 9(a2) and 10(a2,b2)). These conditions favor regional water mass accumulation and dynamic convergence, displacing the earlier steric-driven regime.

3.3.2. ENSO and AMO Teleconnections

Sea-level anomalies in the GoG are strongly modulated by large-scale climate modes, particularly ENSO and the AMO (Figure 13). The Oceanic Niño Index (ONI) reveals that major El Niño events (e.g., 2020–2023) coincide with elevated SLA in the northern GoG, peaking during boreal spring and autumn (Figure 13a). This response stems from a well-established teleconnection: positive SST anomalies in the equatorial Pacific weaken the Atlantic zonal SST gradient, displacing the ITCZ southward and enhancing rainfall and runoff over the GoG. The combined effect of freshwater input and wind-driven steric adjustments modulates SLA, producing seasonal maxima in April in the southern GoG and November in the northern GoG. These peaks primarily result from the lagged response to cumulative freshwater input, enhanced upper-ocean stratification, and fluvial discharge maxima.

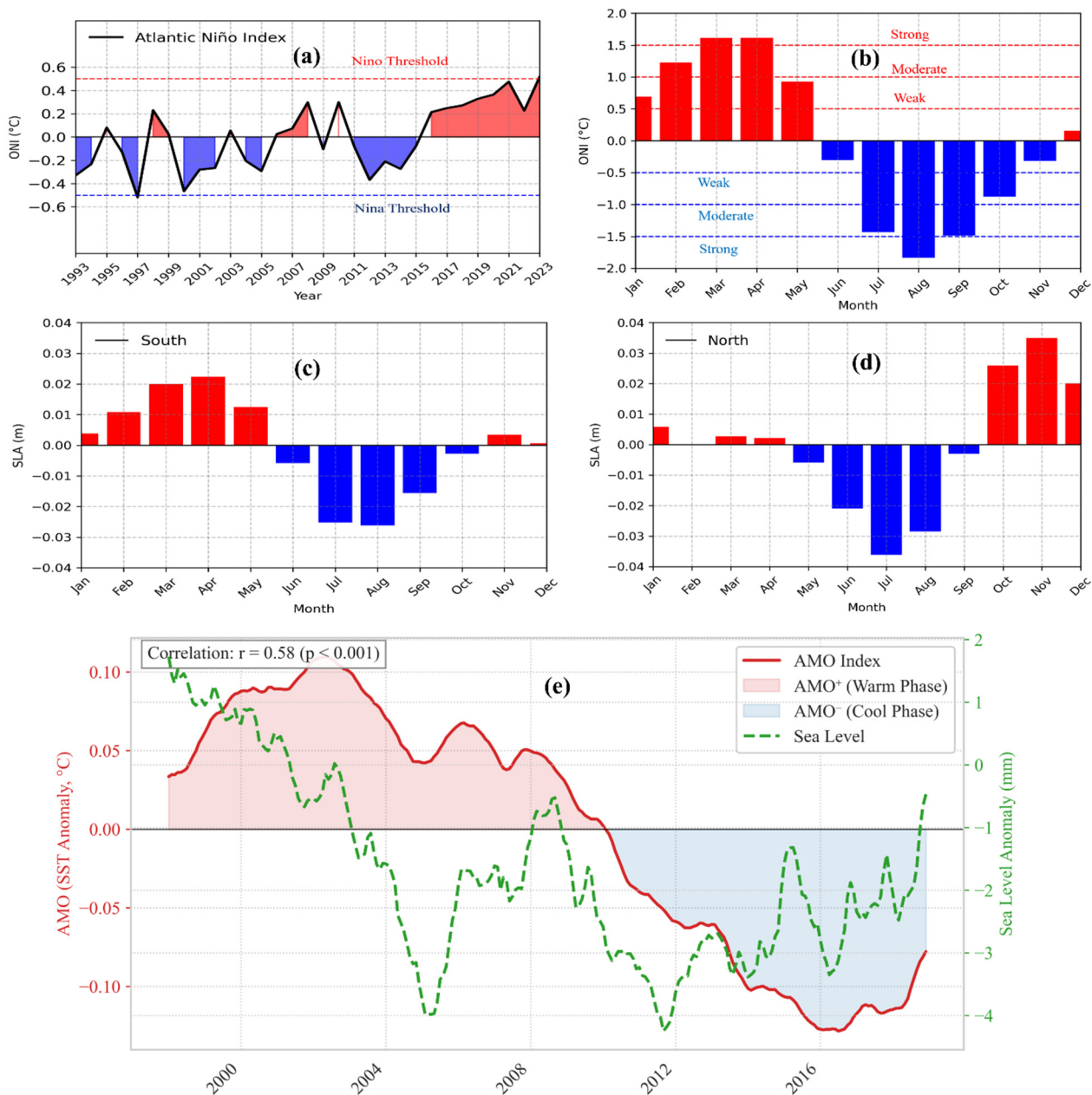


Figure 13. Time series of the Atlantic Niño Index (ONI) from 1993 to 2023, representing the sea surface temperature anomaly in the Atlantic Ocean region (5°S to 5°N, 30°W to 10°W), positive values indicate Niño conditions (red shading), while negative values correspond to Niña conditions (blue shading). The dashed red and blue lines represent threshold values for Niño and Niña events, respectively (a); monthly time series of the ONI. Positive values (shown in red) represent Niño conditions, while negative values (shown in blue) correspond to Niña conditions. The red dashed lines at 0.5, 1.0, and 1.5 denote weak, moderate, and strong Niño thresholds, respectively, while the blue dashed lines at −0.5, −1.0, and −1.5 indicate weak, moderate, and strong Niña conditions (b); monthly time series of the SLA along the northern basin with positive anomalies (shown in red) indicate regions of higher-than-average sea level, while negative anomalies (shown in blue) represent lower-than-average sea level (c); and along the southern basin (d); standardized Atlantic Multidecadal Oscillation (AMO) Index, representing sea surface temperature anomalies in the Atlantic Ocean (0°N–60°N, 80°W–0°W), with a 5-year running mean, and SLA in the Gulf of Guinea (1993–2023) (e).

Hydrological amplification is most pronounced in coastal zones with narrow shelves (e.g., Niger Delta, Bight of Benin), where saturated soils and dense river networks exacerbate runoff during El Niño. Conversely, La Niña phases suppress convection and SLA

through cooler SSTs, strengthened easterlies, and reduced precipitation. This asymmetry underscores the nonlinearity of ENSO–SLA interactions, with El Niño generating larger, spatially coherent anomalies compared to La Niña’s weaker, diffuse signals (Figure 13b–d). Seasonal SLA patterns further reflect these dynamics, with March–May (southern GoG) and September–November (northern GoG) maxima aligning with ENSO-driven hydroclimatic forcing.

The AMO introduces a low-frequency modulation of SLA by altering North Atlantic SSTs, thereby affecting ITCZ position and WAM intensity (Figure 13e). Positive AMO phases, observed during 1993–2003 and 2018–2023, correspond with higher SLA in the GoG. These intervals align with strengthened WAM activity, increased moisture flux, and elevated runoff. In contrast, the intervening cool AMO phase (2005–2017) coincides with depressed SLA, weaker monsoon circulation, and reduced freshwater inflow. The SLA response to AMO operates through both steric and barotropic pathways, with long-term SST anomalies modulating wind stress, rainfall, and upper-ocean stratification across the tropical Atlantic. The co-occurrence of warm ENSO and AMO phases post-2015 contributed to record-high SLA anomalies in the GoG. This constructive interference illustrates the compounding effects of multiscale climate drivers, wherein interannual ENSO pulses are superimposed on the multidecadal AMO background. These compound forcing regimes contribute to SLA variability through synergistic effects on rainfall, runoff, wind stress, and stratification.

4. Discussion

The Gulf of Guinea has experienced a striking acceleration in sea-level rise, with satellite altimetry revealing a statistically significant increase from $2.93 \pm 0.1 \text{ mm yr}^{-1}$ (1993–2014) to $5.4 \pm 0.25 \text{ mm yr}^{-1}$ (2015–2023). This shift reflects a fundamental transition in the region’s sea-level budget, moving from a steric-dominated regime to one where ocean mass redistribution now plays the dominant role. GRACE/GRACE-FO data indicate that mass contributions have risen from $42 \pm 4\%$ to $58 \pm 5\%$ since 2015, with localized mass loading exceeding 10 mm yr^{-1} near the Niger Delta and Cameroon coast. These changes are closely linked to intensified precipitation over adjacent catchments, with post-2015 rainfall trends surpassing 6 mm yr^{-1} , sustaining high soil moisture and enhancing terrestrial freshwater discharge. The Gulf of Guinea has recently been identified as the global maximum in ocean mass increase driven by continental hydrology, underscoring the region’s sensitivity to hydrological forcing [33].

The transition to mass-dominated sea-level rise has been facilitated by a reorganization of regional atmospheric circulation. ERA5 reanalysis shows a marked intensification of zonal winds, with an $18 \pm 4\%$ increase in wind stress, alongside the development of a cyclonic wind stress curl anomaly in the eastern Gulf. These changes have modified coastal dynamics through multiple mechanisms, including enhanced equatorial convergence suppressing offshore Ekman transport, altered reflection characteristics of equatorial waves at the eastern boundary, and increased downwelling-favorable winds along the northern coastline. Collectively, these shifts have disrupted the basin’s waveguide dynamics, reducing thermocline tilting, decreasing Rossby wave speeds, and diminishing coherence between equatorial and coastal sea-level anomalies.

Interannual climate variability interacts with these local processes to generate nonlinear sea-level responses. Strong El Niño events elevate regional sea level through combined steric and manometric mechanisms, while atmospheric teleconnections enhance coastal precipitation and equatorial wind anomalies disrupt wave propagation. The 2022–2023 El Niño, coinciding with a warm AMO phase, produced the largest sea-level excursion of the altimetry era through this coupled mechanism. On decadal scales, the AMO modulates the

background state, with warm phases intensifying precipitation responses to ENSO events and strengthening West African Monsoon circulation, creating sustained conditions for mass loading.

Despite these insights, current climate models continue to underestimate regional sea-level responses, particularly in terrestrial-marine coupling. CMIP6 ensemble members show a 20–45% underestimation of mass contributions, largely due to coarse coastal resolution and oversimplified land hydrology schemes [34,35]. These biases compromise projections of future regional sea-level change, especially as anthropogenic warming intensifies the hydrological cycle and modifies tropical wave dynamics. Key uncertainties remain in isolating the relative roles of internal variability versus anthropogenic forcing in driving observed circulation shifts and in determining whether similar steric-to-mass transitions are occurring in other tropical marginal seas.

5. Conclusions

The Gulf of Guinea has undergone a profound shift in its sea-level regime, transitioning from steric-dominated rise to a mass-driven acceleration, with regional trends now exceeding 5 mm/yr. This change reflects the growing influence of terrestrial hydrology and modified wind-driven circulation, underscoring how coastal sea levels respond to interconnected atmospheric, oceanic, and hydrological processes. While climate modes like ENSO and the AMO amplify extremes, current models systematically underestimate these regional dynamics due to inadequate representation of land-ocean coupling. The region's transformation serves as a critical case study, demonstrating that future sea-level projections must integrate high-resolution coastal processes with large-scale climate forcing. Addressing these gaps through enhanced observations and improved modeling frameworks will be essential for accurate risk assessment and adaptation planning in vulnerable coastal zones worldwide. As anthropogenic warming intensifies the hydrological cycle and alters ocean dynamics, the Gulf of Guinea's experience may foreshadow similar transitions in other tropical marginal seas, making its study vital for anticipating future coastal challenges.

Author Contributions: Conceptualization, H.Y. and A.A.S.; methodology, A.A.S.; software, H.Y.; validation, A.A.S., H.Y., and N.K.; formal analysis, A.A.S.; investigation, H.Y.; resources, K.W.; data curation, A.A.S.; writing—original draft preparation, A.A.S.; writing—review and editing, N.K.; visualization, A.A.S.; supervision, K.W.; project administration, K.W.; funding acquisition, H.Y. All authors have read and agreed to the published version of the manuscript.

Funding: This research received no external funding.

Data Availability Statement: All datasets used in this study are publicly available. Satellite altimetry data were obtained from CMEMS (<https://marine.copernicus.eu>) and AVISO (<https://www.aviso.altimetry.fr>). Reanalysis data were accessed from ERA5 via the Copernicus Climate Data Store (<https://cds.climate.copernicus.eu>). GRACE-FO data were retrieved from NASA (<https://grace.jpl.nasa.gov>). Glacial isostatic adjustment (GIA) corrections follow Peltier (2015) and are publicly available at <http://www.atmosp.physics.utoronto.ca/~peltier/data.php> accessed on 20 June 2024. All data are freely accessible for research purposes.

Conflicts of Interest: The authors declare no conflict of interest.

References

1. Dangendorf, S.; Hay, C.; Calafat, F.M.; Marcos, M.; Piecuch, C.G.; Berk, K.; Jensen, J. Persistent acceleration in global sea-level rise since the 1960s. *Nat. Clim. Change* **2019**, *9*, 705–710. [CrossRef]
2. Oppenheimer, M.; Glavovic, B.; Hinkel, J.; Van de Wal, R.; Magnan, A.K.; Abd-Elgawad, A.; Cai, R.; Cifuentes-Jara, M.; DeConto, R.M.; Ghosh, T.; et al. Sea Level Rise and Implications for Low-Lying Islands, Coasts and Communities. In *IPCC Special Report on the Ocean and Cryosphere in a Changing Climate*; IPCC: Geneva, Switzerland, 2019.

3. Lee, H.; Calvin, K.; Dasgupta, D.; Krinner, G.; Mukherji, A.; Thorne, P.; Trisos, C.; Romero, J.; Aldunce, P.; Barret, K.; et al. *Climate Change 2023: Synthesis Report, Summary for Policymakers. Contribution of Working Groups I, II, and III to the Sixth Assessment Report of the Intergovernmental Panel on Climate Change*; IPCC: Geneva, Switzerland, 2023.
4. Longhurst, A.R. A review of the oceanography of the Gulf of Guinea. *Bull. Inst. Fr. Afr. Noire Sér. A Sci. Nat.* **1962**, *24*, 633–663.
5. Aman, A.; Testut, L.; Woodworth, P.L.; Aarup, A.; Dixon, D.J. Seasonal sea level variability in the Gulf of Guinea from altimetry and tide gauge. *Rev. Ivoir. Sci. Technol.* **2007**, *9*, 105–118.
6. Ayinde, A.S.; Yu, H.; Wu, K. Sea level variability and modeling in the Gulf of Guinea using supervised machine learning. *Sci. Rep.* **2023**, *13*, 21318. [\[CrossRef\]](#)
7. Ghomsi, F.E.K.; Raj, R.P.; Bonaduce, A.; Halo, I.; Nyberg, B.; Cazenave, A.; Rouault, M.; Johannessen, O.M. Sea level variability in Gulf of Guinea from satellite altimetry. *Sci. Rep.* **2024**, *14*, 4759. [\[CrossRef\]](#)
8. Dieng, H.B.; Dadou, I.; Léger, F.; Morel, Y.; Jouanno, J.; Lyard, F.; Allain, D. Sea level anomalies using altimetry, model and tide gauges along the African coasts in the Eastern Tropical Atlantic Ocean: Inter-comparison and temporal variability. *Adv. Space Res.* **2021**, *68*, 534–552. [\[CrossRef\]](#)
9. Evadzi, P.I.K.; Zorita, E.; Hünicke, B. West African sea level variability under a changing climate: What can we learn from the observational period? *J. Coast. Conserv.* **2019**, *23*, 759–771. [\[CrossRef\]](#)
10. Fox-Kemper, B.; Hewitt, H.T.; Xiao, C.; Aðalgeirsdóttir, G.; Drijfhout, S.S.; Edwards, T.L.; Golledge, N.R.; Hemer, M.; Kopp, R.E.; Krinner, G.; et al. Ocean, cryosphere and sea level change. In *Climate Change 2021: The Physical Science Basis*; Cambridge University Press: Cambridge, UK, 2021.
11. Good, S.A.; Martin, M.J.; Rayner, N.A. EN4: Quality controlled ocean temperature and salinity profiles and monthly objective analyses with uncertainty estimates. *J. Geophys. Res. Ocean.* **2013**, *118*, 6704–6716. [\[CrossRef\]](#)
12. Peltier, W.R.; Argus, D.F.; Drummond, R. Space geodesy constrains ice age terminal deglaciation: The global ICE-6G_C (VM5a) model. *J. Geophys. Res. Solid Earth* **2015**, *120*, 450–487. [\[CrossRef\]](#)
13. Mann, H.B. Nonparametric tests against trend. *Econometrica* **1945**, *13*, 245–259. [\[CrossRef\]](#)
14. Kendall, M.G. *Rank Correlation Methods*; Griffin: London, UK, 1975.
15. Sen, P.K. Estimates of the regression coefficient based on Kendall's tau. *J. Am. Stat. Assoc.* **1968**, *63*, 1379–1389. [\[CrossRef\]](#)
16. Theil, H. A Rank-Invariant Method of Linear and Polynomial Regression Analysis. *Proc. Neth. Acad. Arts Sci.* **1950**, *53*, 521–525.
17. Iler, A.M.; Inouye, D.W.; Schmidt, N.M.; Høye, T.T. Detrending phenological time series improves climate–phenology analyses and reveals evidence of plasticity. *Ecology* **2017**, *98*, 647–655. [\[CrossRef\]](#)
18. Lorenz, E.N. Empirical orthogonal functions and statistical weather prediction. In *Statistical Forecasting Project Report 1*; MIT Department of Meteorology: Cambridge, MA, USA, 1956.
19. North, G.R.; Bell, T.L.; Cahalan, R.F.; Moeng, F.J. Sampling errors in the estimation of empirical orthogonal functions. *Mon. Weather Rev.* **1982**, *110*, 699–706. [\[CrossRef\]](#)
20. Von Storch, H.; Zwiers, F.W. *Statistical Analysis in Climate Research*; Cambridge University Press: Cambridge, UK, 2002.
21. Swenson, S.; Chambers, D.; Wahr, J. Estimating geocenter variations from a combination of GRACE and ocean model output. *J. Geophys. Res. Solid Earth* **2008**, *113*, B08410. [\[CrossRef\]](#)
22. Wahr, J.; Molenaar, M.; Bryan, F. Time variability of the Earth's gravity field: Hydrological and oceanic effects and their possible detection using GRACE. *J. Geophys. Res. Solid Earth* **1998**, *103*, 30205–30229. [\[CrossRef\]](#)
23. Chen, X.; Zhang, X.; Church, J.A.; Watson, C.S.; King, M.A.; Monselesan, D.; Legresy, B.; Harig, C. The increasing rate of global mean sea-level rise during 1993–2014. *Nat. Clim. Change* **2017**, *7*, 492–495. [\[CrossRef\]](#)
24. Chelton, D.B.; DeSzoeke, R.A.; Schlax, M.G.; El Naggar, K.; Siwertz, N. Geographical variability of the first baroclinic Rossby radius of deformation. *J. Phys. Oceanogr.* **1998**, *28*, 433–460. [\[CrossRef\]](#)
25. Guiavarc'h, C.; Tréguier, A.M.; Vangriesheim, A. Deep currents in the Gulf of Guinea: Along slope propagation of intraseasonal waves. *Ocean Sci.* **2009**, *5*, 141–153. [\[CrossRef\]](#)
26. Wiafe, G.; Nyadjro, E.S. Satellite observations of upwelling in the Gulf of Guinea. *IEEE Geosci. Remote Sens. Lett.* **2015**, *12*, 1066–1070. [\[CrossRef\]](#)
27. Bouttes, N.; Gregory, J.M.; Kuhlbrodt, T.; Smith, R.S. The drivers of projected North Atlantic sea level change. *Clim. Dyn.* **2014**, *43*, 1531–1544. [\[CrossRef\]](#)
28. Chafik, L.; Nilsen, J.E.; Dangendorf, S.; Reverdin, G.; Frederikse, T. North Atlantic Ocean circulation and decadal sea level change during the altimetry era. *Sci. Rep.* **2019**, *9*, 1041. [\[CrossRef\]](#)
29. Adamec, D.; O'Brien, J.J. The seasonal upwelling in the Gulf of Guinea due to remote forcing. *J. Phys. Oceanogr.* **1978**, *8*, 1050–1060. [\[CrossRef\]](#)
30. Verstraete, J.M. The seasonal upwellings in the Gulf of Guinea. *Prog. Oceanogr.* **1992**, *29*, 1–60. [\[CrossRef\]](#)
31. Thorncroft, C.D.; Nguyen, H.; Zhang, C.; Peyrillé, P. Annual cycle of the West African monsoon: Regional circulations and associated water vapour transport. *Q. J. R. Meteorol. Soc.* **2011**, *137*, 129–147. [\[CrossRef\]](#)

32. Vellinga, M.; Arribas, A.; Graham, R. Seasonal forecasts for regional onset of the West African monsoon. *Clim. Dyn.* **2013**, *40*, 3047–3070. [[CrossRef](#)]
33. McGirr, R.; Tregoning, P.; Purcell, A.; McQueen, H. Significant local sea level variations caused by continental hydrology signals. *Geophys. Res. Lett.* **2024**, *51*, e2024GL108394. [[CrossRef](#)]
34. Slangen, A.B.; Meyssignac, B.; Agosta, C.; Champollion, N.; Church, J.A.; Fettweis, X.; Ligtenberg, S.R.; Marzeion, B.; Melet, A.; Palmer, M.D.; et al. Evaluating model simulations of twentieth-century sea level rise. Part I: Global mean sea level change. *J. Clim.* **2017**, *30*, 8539–8563. [[CrossRef](#)]
35. Meyssignac, B.; Slangen, A.A.; Melet, A.; Church, J.A.; Fettweis, X.; Marzeion, B.; Agosta, C.; Ligtenberg, S.R.M.; Spada, G.; Richter, K.; et al. Evaluating model simulations of twentieth-century sea-level rise. Part II: Regional sea-level changes. *J. Clim.* **2017**, *30*, 8565–8593. [[CrossRef](#)]

Disclaimer/Publisher’s Note: The statements, opinions and data contained in all publications are solely those of the individual author(s) and contributor(s) and not of MDPI and/or the editor(s). MDPI and/or the editor(s) disclaim responsibility for any injury to people or property resulting from any ideas, methods, instructions or products referred to in the content.